Article

Unconventional insulator-to-metal phase transition in Mn₃Si₂Te₆

Yanhong Gu[1], Kevin A. Smith [1], Amartyajyoti Saha [2,3], Chandan De[4,12], Choong-jae Won [4], Yang Zhang [5], Ling-Fang Lin [5], Sang-Wook Cheong [4,6,7], Kristjan Haule [8], Mykhaylo Ozerov [9], Turan Birol [2], Christopher Homes [10], Elbio Dagotto [5,11] & Janice L. Musfeldt [1,5] ✉

The nodal-line semiconductor Mn₃Si₂Te₆ is generating enormous excitment due to the recent discovery of a field-driven insulator-to-metal transition and associated colossal magnetoresistance as well as evidence for a new type of quantum state involving chiral orbital currents. Strikingly, these qualities persist even in the absence of traditional Jahn-Teller distortions and double-exchange mechanisms, raising questions about exactly how and why magnetoresistance occurs along with conjecture as to the likely signatures of loop currents. Here, we measured the infrared response of Mn₃Si₂Te₆ across the magnetic ordering and field-induced insulator-to-metal transitions in order to explore colossal magnetoresistance in the absence of Jahn-Teller and double-exchange interactions. Rather than a traditional metal with screened phonons, the field-driven insulator-to-metal transition leads to a weakly metallic state with localized carriers. Our spectral data are fit by a percolation model, providing evidence for electronic inhomogeneity and phase separation. Modeling also reveals a frequency-dependent threshold field for carriers contributing to colossal magnetoresistance which we discuss in terms of polaron formation, chiral orbital currents, and short-range spin fluctuations. These findings enhance the understanding of insulator-to-metal transitions in new settings and open the door to the design of unconventional colossal magnetoresistant materials.

Phase transitions involving electronic heterogeneity are well-established in quantum materials, as evidenced by the way electron correlations lead to Mott systems with insulator-to-metal transitions[1–3] and low carrier densities generate colossal magnetoresistance (CMR)[4,5]. These principles were explored in nearly Dirac materials like EuMnSb₂[6], Mott insulating Ti-doped Ca₃Ru₂O₇[7], and perovskite manganites such as La₁₋ₓSrₓMnO₃[8,9], and although there is a significant body of work revealing insulator-to-metal transitions triggered by temperature, pressure, and light[10–16], magnetically-driven transitions are particularly attractive due to th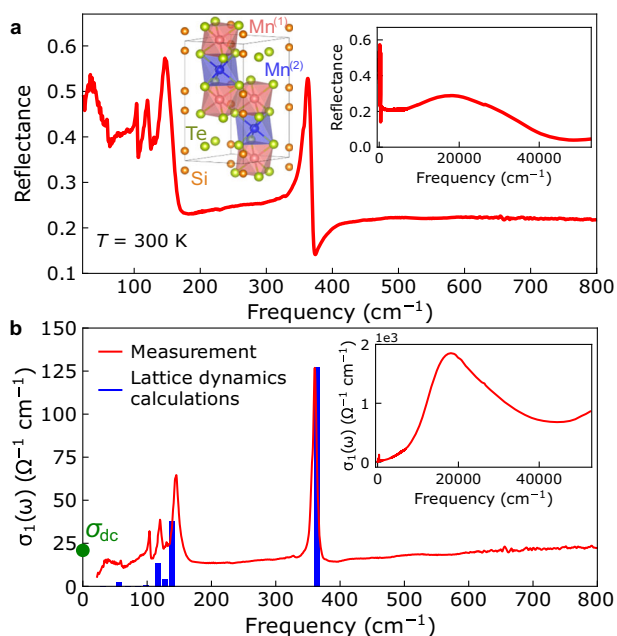eir ability to support CMR. The latter typically relies upon Jahn-Teller distortions and double-exchange mechanisms, although the recent discovery of Mn₃Si₂Te₆ demonstrates that these interactions are not required, while also introducing a novel quantum state involving chiral orbital currents[17] that merits further investigation.

Mn₃Si₂Te₆ hosts trigonal $P\bar{3}1c$ symmetry with two different Mn(II) sites as well as alternately stacked honeycomb and triangular layers[18,19]. This nodal line semiconductor displays an insulator-to-metal transition and CMR under a magnetic field for $H\|c$[20,21]. Significant magnetic anisotropy arises from strong spin-orbit coupling

due to Te orbits coupled with Mn spins; this proximity effect is consistent with strong hybridization between Mn and Te orbitals and is easily perturbed by small *dc* currents[17,20–22]. Whether $Mn_3Si_2Te_6$ hosts a spin-rotation-favored insulator-to-metal transition or chiral orbital current state-induced CMR[17,21], the majority of measurements thus far involve transport techniques, making it difficult to ascertain the microscopic aspects of the electronic response—especially in the presence of a chiral orbital current that might create electronic localization in combination with spin-phonon coupling, topological nodal-line degeneracy, magnetization anisotropy, and magnetic fluctuations[21,23–28]. Questions have therefore arisen about how itinerary and electron correlations compete with localization and whether carriers are created homogeneously as part of the insulator-to-metal transition and CMR effect. Magneto-infrared spectroscopy is a powerful tool for addressing these issues.

In order to unravel the origin of CMR in a material that does not host Jahn-Teller or double-exchange interactions and to search for spectroscopic signatures of chiral loop currents, we measured the infrared response of $Mn_3Si_2Te_6$ across the magnetic ordering and insulator-to-metal transitions. Rather than a conventional metal with a Drude response and screened phonons, the field-driven insulator-to-metal transition leads to a weakly metallic state with localized carriers. We discuss this localization in terms of the large polaron model, expectations for chiral orbital currents, and the ability of short-range spin fluctuations to give rise to Slater peaks[17,29–32]. The dynamics of these pinned carriers are captured by the percolation model, which emphasizes the ubiquity of electronic heterogeneity in CMR systems. In this case, a frequency-dependent threshold magnetic field accounts for the gradual formation of the weakly metallic high field phase. These findings complement the understanding of bad metal behavior in correlated oxides, reinforce the role of new quantum states in field-driven insulator-to-metal transitions and their CMR effects, and pave the way for the development of unconventional CMR materials.
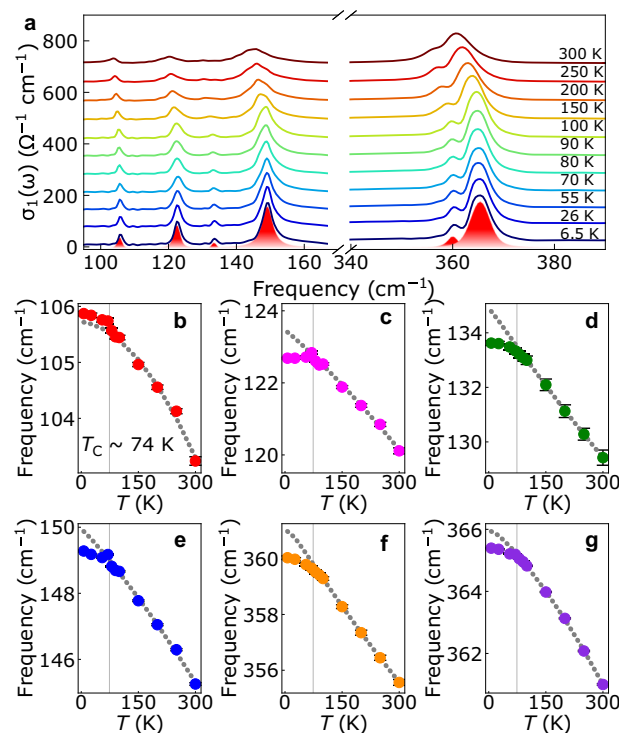
Results and discussion

Classic semiconducting properties at 300 K and across the ferrimagnetic transition

Figure 1 displays the room temperature reflectance of $Mn_3Si_2Te_6$ along with the optical conductivity calculated via Kramers-Kronig analysis. $\sigma_1(\omega)$ is low and flat, characteristic of a semiconductor, punctuated by a series of sharp phonons and localized electronic excitations at higher frequencies[33]. Lattice dynamics calculations allow us to assign the phonons, reveal symmetries, and analyze the displacement patterns [Fig. 1b and Supplementary Table 1, Supplementary Information]. Extrapolation of $\sigma_1(\omega)$ to zero frequency is in reasonable agreement with the *dc* conductivity[20]. The electronic properties are typical of a semiconductor with indirect and direct gaps of 0.43 and 1.73 eV, respectively [Supplementary Note 11]. The gap sizes are similar to those in $CrSiTe_3$ due to the common $[Si_2Te_6]^{6-}$ cluster anion[34,35]. We assign the strong electronic features near 20,000 cm^{-1} shown in the inset to a combination of charge transfer and *d*-to-*d* excitations.

To investigate how strongly these phonons interact with the Mn spin system, we measured the infrared response across the ferrimagnetic ordering transition. Figure 2 summarizes the optical conductivity of $Mn_3Si_2Te_6$ as a function of temperature. Here we show six representative vibrational modes fit by Voigt functions, indicated by the red-shaded area. All of the phonons harden on approach to the magnetic ordering transition [Fig. 2b–g]—a trend that we quantify with a traditional anharmonic model[36,37]. Below $T_C = 74$ K[18], the frequency vs. temperature data deviates from the model curve that typifies the high-temperature phase. This perturbation is characterized by a frequency shift: $\Delta\omega = \lambda\langle S_i \cdot S_j\rangle$, where λ is the spin-phonon coupling constant, and $\langle S_i \cdot S_j\rangle$ is the spin-spin correlation function between the (i,j) nearest neighbors. The latter approaches S^2 in the low-temperature limit. The
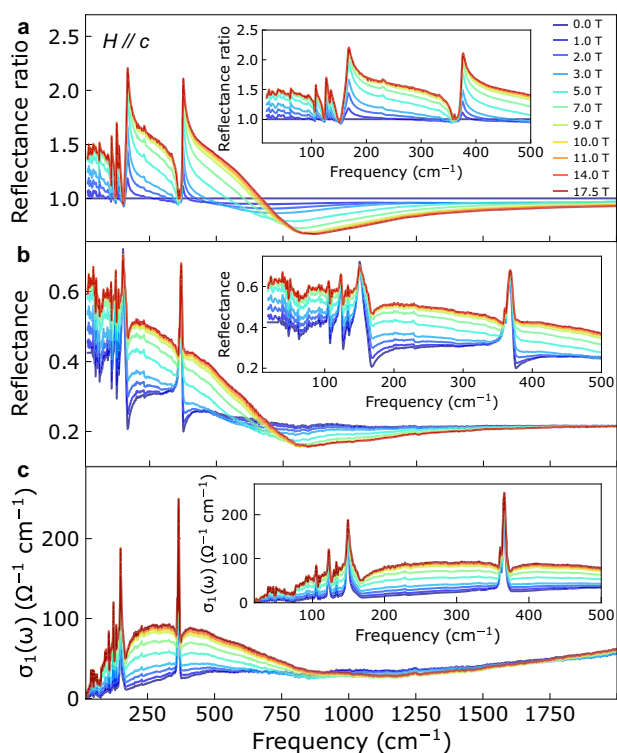

Fig. 1 | Optical properties of $Mn_3Si_2Te_6$ at room temperature. a Reflectance of $Mn_3Si_2Te_6$ in the *ab*-plane at 300 K along with the crystal structure[19] showing two distinct Mn sites. Inset: reflectance over a wide frequency range. **b** Optical conductivity calculated from a Kramers–Kronig analysis of the measured reflectance, predicted pattern of the E_u symmetry phonons from our lattice dynamics calculations (normalized for easy comparison), and *dc* conductivity from ref. 20. Inset: $\sigma_1(\omega)$ over the full range of our measurements.

Fig. 2 | Properties of $Mn_3Si_2Te_6$ across the magnetic ordering transition. a Close-up view of the optical conductivity as a function of temperature. The red shaded area represents the fitting results. The data are offset for clarity. **b–g** Frequency vs. temperature for six representative phonons. Individual points are obtained from fits to $\sigma_1(\omega)$ in **a**, and the dotted lines represent a fit to typical anharmonic behavior[36,37]. The magnetic ordering temperature is indicated by the gray vertical line at 74 K. Unless indicated, error bars are smaller than the symbol size.

spin-phonon coupling constants that we extract for the infrared-active modes are modest—less than $\pm 0.25\,cm^{-1}$ [Supplementary Table 1, Supplementary Information]—similar in size to the λ's for the Raman-active phonons[23]. These values are significantly smaller than those in heavy and mixed-metal oxides[38] ruling out a substantial role for spin-phonon coupling of $q = 0$ phonons in the insulator-to-metal transition and CMR effect.

Bad metal behavior in the high-field phase

Having placed the properties of the semiconducting phase on a firm foundation, we turn our attention to the metallic phase of $Mn_3Si_2Te_6$, using a magnetic field to drive the insulator-to-metal transition. Figure 3a shows the reflectance ratio as a function of magnetic field. This quantity (discussed in Supplementary Note 5) highlights the sharp phonons as well as broad changes in the electronic background. We used these data along with the absolute reflectance at base temperature and zero field to back-calculate the reflectance as a function of magnetic field [Fig. 3b]. The reflectance rises systematically between 3 and 9 T, consistent with transport results that place the insulator-to-metal transition in this range[17,21]. That said, the rise is nowhere near what is expected for a true metal like copper. Instead of developing a signature Drude response, we see over-damped behavior even at full field (17.5 T), characteristic of a bad metal[39,40]. We simulate this effect in Supplementary Note 6. At the same time, the phonons remain prominent and are not well-screened. This reveals that $Mn_3Si_2Te_6$ does not behave as a conventional metal following the field-induced insulator-to-metal transition.
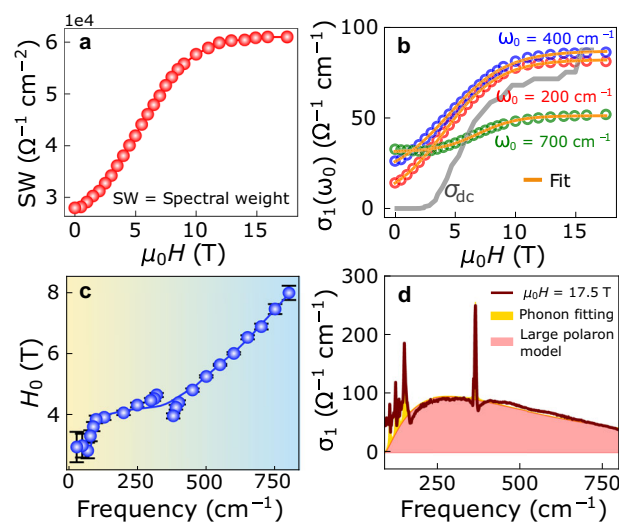
Figure 3c displays the optical conductivity of $Mn_3Si_2Te_6$ across the insulator-to-metal transition. The most striking feature is the build-up of localized excitations with increasing magnetic field rather than the development of a free carrier (Drude) response. Electronic character is demonstrated by the broad energy range as well as the Fano lineshape of the phonons that ride on top of this band in the high field phase[41]. That said, the phonon positions are nearly rigid over the entire field range, excluding the lattice as the origin of these effects. Close-up views of these trends and the near-zero spin-phonon coupling constants that result from the absence of a frequency shift across the field-induced insulator-to-metal transition are given in Supplementary Fig. 6 of the Supplementary Note 7.

We can analyze the electronic properties in greater depth by focusing on charge localization. A sum rule analysis of the low energy localized excitation in $\sigma_1(\omega)$ yields the oscillator strength trend shown in Fig. 4a. The spectral weight, which is proportional to the effective number of carriers, increases rapidly near 5 T and levels off above 10 T. This growth in the number of carriers aligns nicely with the field-driven insulator-to-metal transition and the associated CMR effect. To better connect charge localization, the number of carriers, and CMR, we examined several fixed-frequency cuts of $\sigma_1(\omega)$ along with the dc conductivity from ref. 21. We note in passing that although the field enhances both ac and dc conductivities across the insulator-to-metal transition, the overall magnitude of σ_{dc} in the high field phase is not very large, consistent with our picture of $Mn_3Si_2Te_6$ as a bad metal. Turning back to the analysis of electronic localization in the optical conductivity [Fig. 4b], we see that the ac conductivities at 200 and 400 cm^{-1} vary across the insulator-to-metal transition in a manner similar to (but broader than) the dc conductivity. This makes sense because $\sigma_1(\omega \rightarrow 0)$ is σ_{dc}. By contrast, carriers pinned at 700 cm^{-1} are not nearly as responsive to the transition. These findings suggest that carriers with frequencies below ≈400 cm^{-1} may be the primary contributors to CMR.

Unraveling electronic heterogeneity and localization

Electronic heterogeneity plays a foundational role in establishing the properties of CMR manganites. One way to quantify inhomogeneity and phase separation is with the percolation model[42]. This model,

Fig. 3 | Reflectance and optical conductivity in magnetic field. a Reflectance ratios of $Mn_3Si_2Te_6$ as a function of magnetic field. Inset: close-up view of the reflectance ratio spectra. All data are collected at 5.5 K. As we discuss in the main text, the appearance of new features at high fields is entirely due to changes in the electronic background and is almost totally decoupled from the lattice. **b** Reflectance as a function of magnetic field, back-calculated from the base temperature data in Fig. 2 and the ratios in **a**. Inset: close-up view of the reflectance spectra. **c** Optical conductivity of $Mn_3Si_2Te_6$ as a function of magnetic field, calculated from a Kramers–Kronig analysis of the reflectance in **b**. Inset: close-up view of the optical conductivity in the far infrared range.

Fig. 4 | Revealing the properties of localized carriers. a Spectral weight calculated by integrating $\sigma_1(\omega)$ over an appropriate frequency window. **b** $\sigma_1(\omega)$ at several different fixed frequencies ω_0 (circles) vs. magnetic field. The dark orange lines are fits to the percolation model. The dc conductivity is from ref. 21. **c** Percolation threshold as a function of frequency, obtained from percolation model fits in **b**. **d** $\sigma_1(\omega)$ at 17.5 T fit with a large polaron model (red area) and typical phonon oscillators (yellow area). Unless indicated, the error bars are smaller than the symbol size.

originally developed to describe progressively increasing concentrations of metallic nanoparticles in a dielectric background like glass, has been successfully applied to correlated electron materials like VO_2 across the phase transition[43], WS_2 nanotubes under pressure[44], and rare-earth nickelates like $NdNiO_3$[45]. In these modern settings, the percolation model refers to "droplets" of metallicity embedded in a dielectric matrix (which represents a competing phase), as illustrated in the Supplementary Note 10. To focus on the electronic properties (and avoid the phonons), we employ a single-frequency variant of this approach.

We express the percolation model in fixed frequency form as $\sigma_1(\omega_0) = S_2 + (S_1 - S_2)/(1 + e^{(H-H_0)/\Delta H})$[44]. Here, ω_0 is the fixed frequency in question, and $\sigma_1(\omega_0)$ is a fixed-frequency cut of $\sigma_1(\omega)$. S_1 and S_2 are the fit values of $\sigma_1(\omega_0)$ at 0 and 17.5 T. H_0 defines the percolation threshold at the fixed frequency ω_0. The percolation threshold is the critical magnetic field at which the concentration of the metallic phase rises sufficiently to provide long-range connectivity. This is the parameter that gives physical significance to the model. H is magnetic field, and ΔH represents the slope of the curve (or the range over which percolation persists−from zero to full percolation). As shown in Fig. 4b, trends in $\sigma_1(\omega_0)$ vs. H are perfectly captured with fits to the model, demonstrating that the shape of the insulator-to-metal transition is a consequence of electronic heterogeneity. This means that the insulator-to-metal transition begins with a small amount of metallic phase embedded in a dielectric matrix, and with increasing magnetic field, the concentration of the metallic phase grows while that of the semiconducting phase diminishes. The fact that magnetization is not fully saturated at 17.5 T[20,21,26] is consistent with our picture of an underdeveloped metallic phase above the insulator-to-metal transition.

Figure 4c shows the percolation threshold of $Mn_3Si_2Te_6$ as a function of frequency extracted from the percolation model fits in Fig. 4b. The trend demonstrates that carriers react based on their degree of localization. Low-frequency carriers respond quickly to magnetic fields and reach their percolation threshold by 4 T, whereas the higher-frequency carriers react more slowly and require larger fields to become mobile. In fact, examination reveals that carriers with frequencies below 400 cm^{-1} exhibit a percolation threshold field between 3 and 4 T where dc resistance is already suppressed by >97.5%[20]. On the other hand, carriers above 400 cm^{-1} host percolation thresholds increase with frequency−a tendency that creates an uneven magnetic field response in $\sigma_1(\omega)$ [Fig. 3c]. This distribution of percolation thresholds explains why the insulator-to-metal transition is so broad and why the conductivity is not fully developed even in fields that ought to place the material well above the transition. $Mn_3Si_2Te_6$ is a clean system without mixed valencies or doping, so carriers that are less responsive to applied field are what keep the system in an electronically localized state even above the insulator-to-metal transition.

Modeling the localized excitation: large polaron, chiral loop currents, or short-range spin fluctuations

The field-driven development of the localized electronic excitation suggests that there may be important vibronic interactions or distortions of the magnetic order that pin the charge to the lattice or spin texture in the form of lattice or magnetic polarons[46–48]. A polaronic-like structure has already been observed at lower energies (~40 cm^{-1}) under high fluences[33], making it logical that additional polaronic excitations can be created in this material. Certainly, our measurements reveal strong field-induced charge localization in the optical conductivity, and electron-phonon coupling is evidenced by the Fano line shape of the in-plane Si stretching modes near 365 cm^{-1} [Fig. 3c]. We tested this hypothesis by fitting a large polaron model[29–31] to the optical conductivity of $Mn_3Si_2Te_6$ at 17.5 T. As shown in Fig. 4d, a single large polaron model fits the spectrum reasonably well. We extract a radius of ~6 Å, an effective mass of $1.1m_e$, an absorption threshold of 90 cm^{-1}, and a polaron density of $n_p = 1.8 \times 10^{19}$ cm^{-3}. Within this picture, the

presence of the polaron is attributable to the low carrier density originating from Mn-Te hybridization near the Fermi level[22,49] combined with the overall charge transfer character of the material. The limited mobility of this structure is what constrains the development of a more traditional metallic response, although it is still sufficient to produce a CMR effect. We emphasize that the large polaron model is likely a major simplification and that the shape of the bound state is very sensitive to our choices of polaron size, mass, and density. The impact of these parameters is discussed in Supplementary Note 7. In any case, after revealing the behavior of $Mn_3Si_2Te_6$ in a magnetic field and unveiling a competing state via a percolative process, the next challenge is to study this state further and to render it stable at zero magnetic field by chemical substitution.

The fact that phonons are rigid under a magnetic field suggests that we should consider mechanisms beyond charge or spin polaron models. An alternative framework for understanding the presence of localized carriers in the high field phase of $Mn_3Si_2Te_6$ involves the presence of chiral orbital currents flowing along the edges of the $MnTe_6$ octahedra[17]. The loop currents themselves are presumably in the ab-plane, and the moment is generated along c. Carriers pinned near 300 cm^{-1} are consistent with this picture, and based on the resonance frequency, we expect an average loop size on the order of microns. A similar phase is present in smectic metals where current flowing along specific chains displays localization induced by strong interactions[50]. Time-dependent bistable switching[17] and the slow development of magnetization (while changes in the dc resistivity are sharp)[20] are consistent with this picture.

A different approach to understanding magneto-infrared effects in $Mn_3Si_2Te_6$ involves Slater peaks due to short-range spin excitations. Slater argued[51] that the insulating gap can occur solely due to antiferromagnetic order rather than strong on-site Coulomb repulsion. Such a system is called a Slater insulator. Later theoretical work[32] showed that short-range spin fluctuations are sufficient to produce narrow Slater peaks at the edge of the gap near the metal-insulator transition of the Hubbard model, which almost continuously closes the gap at the metal-insulator transition[32,51]. Such excitations come from short-range order and yield a localized excitation in the optical conductivity. One characteristic of the Slater mechanism is the relative entropy between competing states. Typically, the metallic phase has larger entropy than the insulating phase, although in our case, analysis reveals that the entropies are similar[52,53]. More work is obviously needed to clarify the matter, especially real space spectroscopies to unravel electronic inhomogeneities and neutron scattering to determine whether the localized excitation has a magnetic origin.

Methods

Reflectance measurements
High-quality single crystals of $Mn_3Si_2Te_6$ were grown by flux techniques[21] and polished to expose the ab-plane. Near-normal reflectance was measured between 22 and 55,000 cm^{-1} using a series of spectrometers, and a Kramers-Kronig analysis provided the optical constants[54]. Here, we focus on the real part of optical conductivity ($\sigma_1(\omega)$). Temperature was controlled with an open-flow cryostat. The magnetic field was applied using a 17.5 T superconducting magnet ($H\|c$) at the National High Magnetic Field Laboratory in Tallahassee, FL.

Lattice dynamic calculations
First-principles calculations were performed using density functional theory as implemented in Vienna ab initio simulation package[55–57] with the projector-augmented wave method[57,58] and the Perdew-Burke-Ernzerhof[59] exchange-correlation function. The DFT-D2 method[60] provided the van der Waals correction on a Γ centered $10 \times 10 \times 6$ k-point grid with a plane-wave cutoff energy of 500 eV. The internal coordinates of the experimental structure[19] were relaxed with ferrimagnetic[52] constraints and the vibrational modes were obtained

using the finite difference method. Details are available in Supplementary Information.

Data availability
All raw data generated in this study are provided in the Source Data file. Source data are provided with this paper.

Code availability
All custom codes used in this study are available from the authors upon request.

References

1. McWhan, D. B. et al. Electronic specific heat of metallic Ti-doped V_2O_3. *Phys. Rev. Lett.* **27**, 941–943 (1971).
2. Imada, M., Fujimori, A. & Tokura, Y. Metal-insulator transitions. *Rev. Mod. Phys.* **70**, 1039–1263 (1998).
3. Gray, A. X. et al. Correlation-driven insulator-metal transition in near-ideal vanadium dioxide films. *Phys. Rev. Lett.* **116**, 116403 (2016).
4. Ramirez, A. Colossal magnetoresistance. *J. Condens. Matter Phys.* **9**, 8171 (1997).
5. Majumdar, P. & Littlewood, P. Magnetoresistance in Mn pyrochlore: electrical transport in a low carrier density ferromagnet. *Phys. Rev. Lett.* **81**, 1314–1317 (1998).
6. Sun, Z. et al. Field-induced metal-to-insulator transition and colossal anisotropic magnetoresistance in a nearly Dirac material $EuMnSb_2$. *npj Quantum Mater.* **6**, 94 (2021).
7. Zhu, M. et al. Colossal magnetoresistance in a Mott insulator via magnetic field-driven insulator-metal transition. *Phys. Rev. Lett.* **116**, 216401 (2016).
8. Urushibara, A. et al. Insulator-metal transition and giant magnetoresistance in $La_{1-x}Sr_xMnO_3$. *Phys. Rev. B* **51**, 14103–14109 (1995).
9. Cooper, S. L. Optical spectroscopic studies of metal-insulator transitions in perovskite-related oxides, 161–219 (Springer Berlin Heidelberg, Berlin, Heidelberg, 2001).
10. Kuneš, J. et al. Metal-insulator transition in $NiS_{2-x}Se_x$. *Phys. Rev. B* **81**, 035122 (2010).
11. Kuwahara, H., Tomioka, Y., Asamitsu, A., Moritomo, Y. & Tokura, Y. A first-order phase transition induced by a magnetic field. *Science* **270**, 961–963 (1995).
12. Kübler, C. et al. Coherent structural dynamics and electronic correlations during an ultrafast insulator-to-metal phase transition in VO_2. *Phys. Rev. Lett.* **99**, 116401 (2007).
13. Inoue, I. H., Goto, O., Makino, H., Hussey, N. E. & Ishikawa, M. Bandwidth control in a perovskite-type $3d^1$-correlated metal $Ca_{1-x}Sr_xVO_3$. I. Evolution of the electronic properties and effective mass. *Phys. Rev. B* **58**, 4372–4383 (1998).
14. Nakamura, F. et al. From Mott insulator to ferromagnetic metal: a pressure study of Ca_2RuO_4. *Phys. Rev. B* **65**, 220402 (2002).
15. Lee, J. S., Krockenberger, Y., Takahashi, K. S., Kawasaki, M. & Tokura, Y. Insulator-metal transition driven by change of doping and spin-orbit interaction in Sr_2IrO_4. *Phys. Rev. B* **85**, 035101 (2012).
16. Feng, Y. et al. A continuous metal-insulator transition driven by spin correlations. *Nat. Commun.* **12**, 2779 (2021).
17. Zhang, Y. et al. Control of chiral orbital currents in a colossal magnetoresistance material. *Nature* **611**, 467–472 (2022).
18. Liu, Y. & Petrovic, C. Critical behavior and magnetocaloric effect in $Mn_3Si_2Te_6$. *Phys. Rev. B* **98**, 064423 (2018).
19. Vincent, H., Leroux, D., Bijaoui, D., Rimet, R. & Schlenker, C. Crystal structure of $Mn_3Si_2Te_6$. *J. Solid State Chem.* **63**, 349–352 (1986).
20. Ni, Y. et al. Colossal magnetoresistance via avoiding fully polarized magnetization in the ferrimagnetic insulator $Mn_3Si_2Te_6$. *Phys. Rev. B* **103**, L161105 (2021).
21. Seo, J. et al. Colossal angular magnetoresistance in ferrimagnetic nodal-line semiconductors. *Nature* **599**, 576–581 (2021).
22. Zhang, Y., Lin, L.-F., Moreo, A. & Dagotto, E. Electronic structure, magnetic properties, spin orientation, and doping effect in $Mn_3Si_2Te_6$. *Phys. Rev. B* **107**, 054430 (2023).
23. Kwon, C. I. et al. Raman signatures of spin-phonon coupling in a self-intercalated van der Waals magnet $Mn_3Si_2Te_6$. *Curr. Appl. Phys.* **53**, 51–55 (2023).
24. Mijin, S. D. et al. Spin-phonon interaction and short-range order in $Mn_3Si_2Te_6$. *Phys. Rev. B* **107**, 054309 (2023).
25. Olmos, R. et al. Critical phenomena of the layered ferrimagnet $Mn_3Si_2Te_6$ following proton irradiation. *J. Appl. Phys.* **130**, 013902 (2021).
26. Ye, F. et al. Magnetic structure and spin fluctuations in the colossal magnetoresistance ferrimagnet $Mn_3Si_2Te_6$. *Phys. Rev. B* **106**, L180402 (2022).
27. Martinez, L. M. et al. Coherent spin-phonon coupling in the layered ferrimagnet $Mn_3Si_2Te_6$. *arXiv* https://arxiv.org/abs/2308.14931 (2023).
28. Zhang, Y. et al. Current-sensitive Hall effect in a chiral-orbital-current state. *Nat. Commun.* **15**, 3579 (2024).
29. Emin, D. Optical properties of large and small polarons and bipolarons. *Phys. Rev. B* **48**, 13691 (1993).
30. Dixit, A., Chen, P., Lawes, G. & Musfeldt, J. L. Electronic structure and polaronic excitation in $FeVO_4$. *Appl. Phys. Lett.* **99**, 141908 (2011).
31. Hartinger, C., Mayr, F., Deisenhofer, J., Loidl, A. & Kopp, T. Large and small polaron excitations in $La_{2/3}(Sr/Ca)_{1/3}MnO_3$ films. *Phys. Rev. B* **69**, 100403 (2004).
32. Park, H., Haule, K. & Kotliar, G. Cluster dynamical mean field theory of the Mott transition. *Phys. Rev. Lett.* **101**, 186403 (2008).
33. Wu, Q. et al. Pump-induced terahertz conductivity response and peculiar bound state in $Mn_3Si_2Te_6$. *Adv. Opt. Mater.* **12**, 2301863 (2023).
34. Siberchicot, B., Jobic, S., Carteaux, V., Gressier, P. & Ouvrard, G. Band structure calculations of ferromagnetic chromium tellurides $CrSiTe_3$ and $CrGeTe_3$. *J. Phys. Chem.* **100**, 5863–5867 (1996).
35. Casto, L. et al. Strong spin-lattice coupling in $CrSiTe_3$. *APL Mater.* **3**, 041515 (2015).
36. Balkanski, M., Wallis, R. & Haro, E. Anharmonic effects in light scattering due to optical phonons in silicon. *Phys. Rev. B* **28**, 1928 (1983).
37. Gu, Y. et al. Phonon mixing in the charge density wave state of ScV_6Sn_6. *npj Quantum Mater.* **8**, 58 (2023).
38. Park, K. et al. Spin–phonon interactions and magnetoelectric coupling in $Co_4B_2O_9$ (B= Nb, Ta). *Appl. Phys. Lett.* **122**, 182902 (2023).
39. Gervais, F. Optical conductivity of oxides. *Mater. Sci. Eng. R: Rep.* **39**, 29–92 (2002).
40. Petit, N., Soret, J.-C. & Gervais, F. Analysis of concentration dependence of optical conductivity of $BaPb_{1-x}Bi_xO_3$ revisited. *Solid State Commun.* **110**, 621–626 (1999).
41. Fano, U. Effects of configuration interaction on intensities and phase shifts. *Phys. Rev.* **124**, 1866–1878 (1961).
42. Carr, G., Perkowitz, S. & Tanner, D. Far-infrared properties of inhomogeneous materials. *Infrared Millim. Waves* **13**, 171–263 (1985).
43. Qazilbash, M. M. et al. Mott transition in VO_2 revealed by infrared spectroscopy and nano-imaging. *Science* **318**, 1750–1753 (2007).
44. O'Neal, K. R. et al. High pressure vibrational properties of WS_2 nanotubes. *Nano Lett.* **16**, 993–999 (2016).
45. Preziosi, D. et al. Direct mapping of phase separation across the metal–insulator transition of $NdNiO_3$. *Nano Lett.* **18**, 2226–2232 (2018).
46. Furdyna, J. K. Diluted magnetic semiconductors. *J. Appl. Phys.* **64**, R29–R64 (1988).
47. Kuivalainen, P., Sinkkonen, J. & Stubb, T. Magnetic polarons in magnetic semiconductors. *Int. J. Quantum Chem.* **20**, 507–519 (1981).

48. Kozyrev, N. et al. Optical manifestation of magnetic polarons bound to excitons and resident holes in a (Cd, Mn) Te quantum well. *Phys. Rev. B* **104**, 045307 (2021).

49. Bigi, C. et al. Covalency, correlations, and interlayer interactions governing the magnetic and electronic structure of $Mn_3Si_2Te_6$. *Phys. Rev. B* **108**, 054419 (2023).

50. Donos, A. & Hartnoll, S. A. Interaction-driven localization in holography. *Nat. Phys.* **9**, 649–655 (2013).

51. Slater, J. C. Magnetic effects and the Hartree-Fock equation. *Phys. Rev.* **82**, 538–541 (1951).

52. May, A. F. et al. Magnetic order and interactions in ferrimagnetic $Mn_3Si_2Te_6$. *Phys. Rev. B* **95**, 174440 (2017).

53. Liu, Y. et al. Polaronic transport and thermoelectricity in $Mn_3Si_2Te_6$ single crystals. *Phys. Rev. B* **103**, 245122 (2021).

54. Wooten, F. Optical properties of solids (*Academic Press*, 1972).

55. Kresse, G. & Furthmüller, J. Efficiency of ab-initio total energy calculations for metals and semiconductors using a plane-wave basis set. *Comput. Mater. Sci.* **6**, 15–50 (1996).

56. Kresse, G. & Furthmüller, J. Efficient iterative schemes for ab initio total-energy calculations using a plane-wave basis set. *Phys. Rev. B* **54**, 11169–11186 (1996).

57. Kresse, G. & Joubert, D. From ultrasoft pseudopotentials to the projector augmented-wave method. *Phys. Rev. B* **59**, 1758 (1999).

58. Blöchl, P. E. Projector augmented-wave method. *Phys. Rev. B* **50**, 17953 (1994).

59. Perdew, J. P., Burke, K. & Ernzerhof, M. Generalized gradient approximation made simple. *Phys. Rev. Lett.* **77**, 3865 (1996).

60. Grimme, S. Semiempirical GGA-type density functional constructed with a long-range dispersion correction. *J. Comput. Chem.* **27**, 1787–1799 (2006).

Acknowledgements

Author contributions

Y.G. and J.L.M. designed the study. C.D., C.W., and S.W.C. grew and characterized the crystals. Y.G. and C.H. studied sample aging and developed techniques to eliminate the surface TeO_2 layer. Y.G. carried out reflectance measurements as a function of temperature. Y.G., K.S., M.O., and J.L.M. performed the magneto-infrared measurements. A.S., Y.Z., and L.F.L. performed lattice dynamics calculations and discussed the results with T.B. and E.D. Y.G. analysed the spectral data with guidance from J.L.M. S.W.C., E.D., and J.L.M. guided the discussion of percolation theory, Y.G. carried out the fits, and K.H. evaluated the Slater mechanism. Y.G., A.S., and J.L.M. wrote the manuscript. All authors commented on the text.

Competing interests

The authors declare no competing interests.

Additional information

Supplementary information The online version contains supplementary material available at https://doi.org/10.1038/s41467-024-52350-1.

Correspondence and requests for materials should be addressed to Janice L. Musfeldt.

Peer review information *Nature Communications* thanks the anonymous reviewers for their contribution to the peer review of this work. A peer review file is available.

Reprints and permissions information is available at http://www.nature.com/reprints

Publisher's note Springer Nature remains neutral with regard to jurisdictional claims in published maps and institutional affiliations.

[1]Department of Chemistry, University of Tennessee, Knoxville, TN 37996, USA. [2]Department of Chemical Engineering and Materials Science, University of Minnesota, Minneapolis, MN 55455, USA. [3]School of Physics and Astronomy, University of Minnesota, Minneapolis, MN 55455, USA. [4]Laboratory for Pohang Emergent Materials and Max Plank POSTECH Center for Complex Phase Materials, Department of Physics, Pohang University of Science and Technology, Pohang 37673, Korea. [5]Department of Physics and Astronomy, University of Tennessee, Knoxville, TN 37996, USA. [6]Department of Physics and Astronomy, Rutgers University, Piscataway, NJ 08854, USA. [7]Rutgers Center for Emergent Materials, Rutgers University, Piscataway, NJ 08854, USA. [8]Center for Materials Theory and Department of Physics and Astronomy, Rutgers University, Piscataway, NJ 08854, USA. [9]National High Magnetic Field Laboratory, Florida State University, Tallahassee, FL 32310, USA. [10]National Synchrotron Light Source II, Brookhaven National Laboratory, Upton, NY 11973, USA. [11]Materials Science and Technology Division, Oak Ridge National Laboratory, Oak Ridge, TN 37831, USA. [12]Present address: Quantum Materials Science Unit, Okinawa Institute of Science and Technology, Okinawa 904-0495, Japan. ✉e-mail: musfeldt@tennessee.edu